

Article

## Non-Classical Single-State Reactivity of an Oxo-Iron(IV) Complex Confined to Triplet Pathways

Claudia Kupper, Bhaskar Mondal, Joan Serrano-Plana, Iris Klawitter, Frank Neese, Miquel Costas, Shengfa Ye, and Franc Meyer

*J. Am. Chem. Soc.*, **Just Accepted Manuscript** • Publication Date (Web): 30 May 2017

Downloaded from <http://pubs.acs.org> on May 30, 2017

### Just Accepted

“Just Accepted” manuscripts have been peer-reviewed and accepted for publication. They are posted online prior to technical editing, formatting for publication and author proofing. The American Chemical Society provides “Just Accepted” as a free service to the research community to expedite the dissemination of scientific material as soon as possible after acceptance. “Just Accepted” manuscripts appear in full in PDF format accompanied by an HTML abstract. “Just Accepted” manuscripts have been fully peer reviewed, but should not be considered the official version of record. They are accessible to all readers and citable by the Digital Object Identifier (DOI®). “Just Accepted” is an optional service offered to authors. Therefore, the “Just Accepted” Web site may not include all articles that will be published in the journal. After a manuscript is technically edited and formatted, it will be removed from the “Just Accepted” Web site and published as an ASAP article. Note that technical editing may introduce minor changes to the manuscript text and/or graphics which could affect content, and all legal disclaimers and ethical guidelines that apply to the journal pertain. ACS cannot be held responsible for errors or consequences arising from the use of information contained in these “Just Accepted” manuscripts.

# Non-Classical Single-State Reactivity of an Oxo-Iron(IV) Complex Confined to Triplet Pathways

Claudia Kupper,<sup>†</sup> Bhaskar Mondal,<sup>‡</sup> Joan Serrano-Plana,<sup>§</sup> Iris Klawitter,<sup>†</sup> Frank Neese,<sup>‡</sup> Miquel Costas,<sup>§</sup> Shengfa Ye,<sup>‡\*</sup> and Franc Meyer<sup>†\*</sup>

<sup>†</sup>Universität Göttingen, Institut für Anorganische Chemie, Tammannstrasse 4, 37077 Göttingen, Germany.

<sup>‡</sup>Max-Planck Institut für Chemische Energiekonversion, Stiftstrasse 34-36, 45470 Mülheim an der Ruhr, Germany.

<sup>§</sup>Institut de Química Computacional i Catàlisi (IQCC), Departament de Química, Universitat de Girona, Campus Montilivi, E17071 Girona, Catalonia, Spain.

<sup>†\*</sup>These authors contributed equally to this work.

**ABSTRACT:** C–H bond activation mediated by oxo-iron(IV) species represents the key step of many heme and non-heme O<sub>2</sub>-activating enzymes. Of crucial interest is the effect of spin state of the Fe<sup>IV</sup>(O) unit. Here we report the C–H activation kinetics and corresponding theoretical investigations of an exclusive tetracarbene ligated oxo-iron(IV) complex, [<sup>NHC</sup>LFe<sup>IV</sup>(O)(MeCN)]<sup>2+</sup> (**1**). Kinetic traces using substrates with bond dissociation energies (BDEs) up to 80 kcal mol<sup>-1</sup> show pseudo-first order behavior and large but temperature-dependent kinetic isotope effects (KIE 32 at -40°C). When compared with a topologically related oxoiron(IV) complex bearing an equatorial N-donor ligand, [<sup>TMCL</sup>LFe<sup>IV</sup>(O)(MeCN)]<sup>2+</sup> (**A**), the tetracarbene complex **1** is significantly more reactive with second order rate constants *k*'<sub>2</sub> that are 2-3 orders of magnitude higher. UV-vis experiments in tandem with cryospray mass spectrometry evidence that the reaction occurs via formation of a hydroxo-iron(III) complex (**4**) after the initial H-atom transfer (HAT). An extensive computational study using a wave function based multireference approach, viz. complete active space self-consistent field (CASSCF) followed by *N*-electron valence perturbation theory up to second order (NEVPT2), provided insight into the HAT trajectories of **1** and **A**. Calculated free energy barriers for **1** reasonably agree with experimental values. Because the strongly donating equatorial tetracarbene pushes the Fe-*d*<sub>x<sup>2</sup>-y<sup>2</sup> orbital above *d*<sub>z<sup>2</sup>, **1** features a dramatically large quintet-triplet gap of ~18 kcal/mol compared to ~2–3 kcal/mol computed for **A**. Consequently, the HAT process performed by **1** occurs on the triplet surface only, in contrast to complex **A** reported to feature two-state-reactivity with contributions from both triplet and quintet states. Despite this, the reactive Fe<sup>IV</sup>(O) units in **1** and **A** undergo the same electronic-structure changes during HAT. Thus, the unique complex **1** represents a pure 'triplet-only' ferryl model.</sub></sub>

## INTRODUCTION

High-valent oxo-iron(IV) species occur in nature as key intermediates in catalytic cycles of numerous heme and non-heme iron enzymes, such as Cytochrome P450, TauD, CytC3 and PheH.<sup>1</sup> Since these species mediate challenging substrate transformations including the oxygenation of unactivated C–H bonds, they are of tremendous interest. Inspired by the biological archetypes, synthetic oxo-iron(IV) complexes are increasingly employed in C-H bond activation chemistry. Over the years, the reactivity of numerous model complexes featuring multidentate chelating *N*-donor coordination has been investigated in great detail.<sup>2</sup> Those studies have shown that the reactivity of oxo-iron(IV) complexes with respect to oxygen atom transfer (OAT), hydrogen atom transfer (HAT), and electron transfer (ET) processes is markedly affected by the supporting ligands and the spin-state of iron.<sup>3</sup>

However, the exact influence of the spin state in non-heme iron systems is still under current debate. Density functional theory (DFT) calculations have predicted a higher reactivity of high-spin ferryl species in the quintet state (*S* = 2) compared to the triplet state (*S* = 1) due to the availability of an additional channel for the approach of the substrate C–H bond to the Fe<sup>IV</sup>(O) unit and a lower activation barrier.<sup>4</sup> Although recent

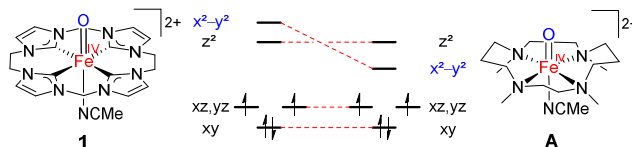
experimental work on dinuclear iron complexes provided support for this theoretical prediction,<sup>5</sup> till date all *S* = 2 mononuclear models available suffer from low stability and/or their reactivity is affected by steric hindrance. The most thoroughly studied high spin Fe<sup>IV</sup>(O) model is so sterically hindered by its TMG<sub>3</sub>tren ligand system (TMG<sub>3</sub>tren = 1,1,1-tris{2-[*N*'<sup>2</sup>-(1,1,3,3-tetramethylguanidino)]ethyl}amine) that it shows reactivity similar to *S* = 1 models.<sup>6,3d</sup> Furthermore, the so far most reactive high spin complex [(TQA)Fe<sup>IV</sup>(O)(NCMe)]<sup>2+</sup> (TQA = tris(quinolin-2-ylmethyl)amine) is only slightly more reactive than its most effective low spin counterpart [(Me<sub>3</sub>NTB)Fe<sup>IV</sup>(O)]<sup>2+</sup> (Me<sub>3</sub>NTB = tris((1-methyl-1H-benzo[d]imidazole-2-yl)methyl)amine), and both species show the same reaction mechanisms and reactivity patterns.<sup>7</sup> Moreover, gas phase reactivity studies on [(PyTACN)Fe=O(X)] compounds (PyTACN = 1-(2'-pyridylmethyl)-4,7-dimethyl-1,4,7-triazacyclononane; X = OTf<sup>-</sup>, ClO<sub>4</sub><sup>-</sup>, CF<sub>3</sub>COO<sup>-</sup>, NO<sub>3</sub><sup>-</sup>) have shown that the nature of the coordinating anions X has a more dramatic effect on the reactivity than the spin state.<sup>8</sup>

Unambiguous comparison of the reactivity of models in triplet and quintet ground states is usually hampered by the classical 'two-state-reactivity' (TSR),<sup>9</sup> a result of the small energy gap between the triplet (*S* = 1) ground state and the quintet (*S*

= 2) excited state in several oxo-iron(IV) model systems. Initiated by interaction with the substrate, the spin state of the system changes when approaching the transition state (TS) and the reaction then proceeds via the quintet surface with a markedly lower activation barrier. However, experimental methods to test such computational predictions are very limited. Recently it has been proposed that the H/D kinetic isotope effect (KIE) may serve as a sensitive mechanistic probe of the spin state pathway during C–H activation by non-heme Fe<sup>IV</sup>(O) complexes, with very large non-classical KIEs indicating  $S = 1$  as the reactive spin state.<sup>10</sup> Evaluation of KIEs for a series of  $S = 1$  Fe<sup>IV</sup>(O) complexes with different supporting ligands and in combinations with different substrates suggested various factors to contribute to the extent of TSR as well as to extent of tunneling, the latter rendering the  $S = 1$  HAT process more favorable.<sup>11</sup> In that situation, a benchmark non-heme Fe<sup>IV</sup>(O) complex whose reactivity is confined to single-state pathways and that can serve as a ‘triplet-only’ model seems highly desirable. Unfortunately though, all common intermediate spin ( $S = 1$ ) systems typically show a small energetic triplet-quintet separation and are thus potentially amenable to TSR.

In 2013, one of our groups prepared and characterized a unique example of an oxo-iron(IV) compound ligated by a macrocyclic tetracarbene ligand, [L<sup>NHC</sup>Fe<sup>IV</sup>(O)(MeCN)]<sup>2+</sup> (**1**) (L<sup>NHC</sup> = 3,9,14,20-tetraaza-1,6,12,17-tetraazoniapentacyclohexacosane-1(23),4,6(26),10,12(25),15,17(24),21-octaene), which is the only authenticated organometallic oxo-iron(IV) published so far.<sup>12</sup> Complex **1** is topologically related to the prominent cyclam-based oxo-iron(IV) complex [L<sup>TMC</sup>Fe<sup>IV</sup>(O)(MeCN)]<sup>2+</sup> (**A**) (L<sup>TMC</sup> = 1,4,8,11-tetramethyl-1,4,8,11-tetraaza-cyclotetradecane),<sup>13</sup> but is electronically distinct. A recent in-depth electronic-structure investigation by using helium tagging infrared photodissociation (IRPD), absorption and magnetic circular dichroism (MCD) spectroscopy in combination with DFT and highly correlated wave function based multireference calculations revealed that the equatorial tetracarbene ligand in **1** does barely affect the bonding in the Fe<sup>IV</sup>(O) unit. However, the very strong equatorial carbene  $\sigma$ -donors push up the  $d_{x^2-y^2}$  orbital to an extent that it lies higher in energy than the  $d_{z^2}$ . The Fe–O stretching vibrations of complex **1** are very similar to that of **A**, not only in the ground state (**1**: 832 cm<sup>-1</sup>; **A**: 834 cm<sup>-1</sup>)<sup>14,15</sup> but also in the excited state that arises from lifting an electron from the nonbonding  $d_{xy}$  orbital into the Fe–O  $\pi^*$  orbitals ( $d_{xz}/d_{yz}$ ) (**1**: 616 cm<sup>-1</sup>; **A**: 610 cm<sup>-1</sup>).<sup>14,16</sup> More importantly, starting from the same electron donating orbitals (EDOs),  $d_{xz}/d_{yz}$ , the excitations to  $d_{z^2}$  feature nearly identical energies for both complexes (~17000 cm<sup>-1</sup>), but the excitations to  $d_{x^2-y^2}$  are found to have a much higher energy for complex **1** (24300 cm<sup>-1</sup>) than that for **A** (12900 cm<sup>-1</sup>). All observations point to distinct ligand-field-splitting patterns for complexes **1** and **A** as sketched in Scheme 1. As a consequence, the substantial geometric changes associated with occupation of the Fe–O  $\sigma^*$  orbital ( $d_{z^2}$ ) on the quintet excited state rationalize a very large triplet-quintet energy gap (18.6 kcal/mol) calculated for **1**. This can be expected to translate into pure triplet-state reactivity, because the quintet state is essentially inaccessible.

**Scheme 1. Structures and Ground-State Electronic Configuration of **1**<sup>12,14</sup> (Left) and **A**<sup>13</sup> (Right).**

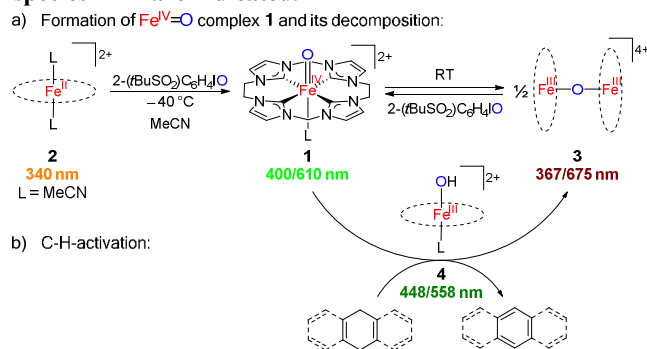


We herein present a combined experimental and theoretical investigation of the reactivity of the unique organometallic Fe<sup>IV</sup>(O) complex **1** towards a set of substrates featuring varying C–H bond dissociation energies (BDE). In order to examine how the triplet-state reactivity of the complex **1** compares with the well-established TSR, we chose the electronically distinct complex **A**, a representative example for classical oxo-iron(IV) compounds in tetragonal ligand field that feature a rather small triplet-quintet energy gap allowing for TSR.<sup>9</sup> In principle, the different electronic structures determined for complexes **1** and **A** may lead to disparate reaction mechanisms for a given transformation. Therefore, a fair comparison of their reactivity is possible only if the HAT reactions with both complexes follow the same mechanism. To this end, we performed a detailed computational study by using density functional theory (DFT) and wavefunction based multireference approaches to evaluate the HAT reactivity of complexes **1** and **A**, and to dissect the electronic-structure changes along their HAT trajectories. As will be shown, comparison of these closely related systems, viz. complexes **1** and **A** provides direct insight into the importance of spin-state on reactivity of oxo-iron(IV) compounds, with **1** representing a benchmark model for pure, intrinsic  $S = 1$  reactivity of ferryl species.

## RESULTS AND DISCUSSION

**C–H bond activation by complex 1.** As shown in Scheme 2, tetracarbene coordinated oxo-iron(IV) complex **1** was generated *in situ* using the soluble iodosobenzene derivative 2-(*t*BuSO<sub>2</sub>)C<sub>6</sub>H<sub>4</sub>-IO following procedures described previously.<sup>12</sup> Complex **1** was found to react with various substrates with relatively weak C–H bonds such as 1,4-cyclohexadiene (CHD), 9,10-dihydroanthracene (DHA), 9*H*-xanthene and 9*H*-fluorene. Reactions were performed in acetonitrile (1 mM) at –40 °C in order to avoid any competing self-decay of **1** to the  $\mu$ -oxo diiron(III) species **3**; under these conditions the reaction progress for the C–H activation can be conveniently monitored.

**Scheme 2. Formation of **1** (a) and its reaction with C–H substrates such as CHD and DHA (b); absorption maxima of species **1** – **4** are indicated.**



Changes observed in UV-vis absorption spectra during the reaction of **1** with CHD (50 equiv) are shown in Figure 1 as a representative example. The initial spectrum shows the characteristic bands of **1** at 400 and 610 nm (light green). Upon addition of substrate, the UV-vis features start changing and two reaction steps can be differentiated while the reaction proceeds. During the first 100 seconds, new features at  $\lambda_{\text{max}} = 367, 448$  and 558 nm for an intermediate **4** appear and reach their maximum absorbance. In a second stage, the bands at  $\lambda_{\text{max}} = 448$  and 558 nm start decreasing whereas the band at  $\lambda_{\text{max}} = 367$  nm keeps rising and a new band at 675 nm emerges (300 s shown in Figure 1, right). This second process continues slowly and the absorbance at 448 nm almost vanishes leading to a final spectrum that is characteristic for the  $\mu$ -oxo diiron(III) complex **3**. Treatment of the data as two sequential processes enables the detection of isosbestic points at 379 and 613 nm during the second step (Figure 1, right).

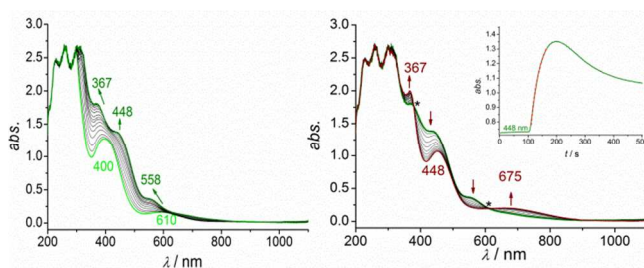


**Figure 1.** UV-vis spectral changes observed upon reaction of **1** (1 mM) with 50 equivalents CHD at  $-40$  °C in acetonitrile during the initial step (about 100 s; left) and the second process (right). Inset: Kinetic trace at 448 nm for this transformation and exponential fit (red dashed line). \* indicates isosbestic points.

Intermediate **4** is assigned to a hydroxo-iron(III) species (Scheme 2) which is generally accepted in literature to form during the first mechanistic step upon abstraction of a substrate H-atom by the oxo-iron(IV) complex.<sup>2,3b,17,18</sup> Supporting evidence for this assignment comes from cryospray mass spectrometry experiments (Figure 2). To that end, **1** was generated at  $-40$  °C in acetonitrile and its initial mass spectrum was recorded. Then, CHD (100 equiv) was added and the evolution of the mass spectrum was followed over time. The initial spectrum of **1** shows two main peaks at  $m/z = 210.1$  ( $[\text{L}^{\text{NHC}}\text{Fe}(\text{O})]^{2+}$ ) and 569.1 ( $[\text{L}^{\text{NHC}}\text{Fe}(\text{O})(\text{OTf})]^{+}$ ). Upon substrate addition, a significant increase of the peaks at  $m/z = 210.6$  and 570.1 corresponding to species  $[\text{L}^{\text{NHC}}\text{Fe}(\text{OH})]^{2+}$  and  $[\text{L}^{\text{NHC}}\text{Fe}(\text{OH})(\text{OTf})]^{+}$  are observed and reach their maximum intensity after around 100 s, in accordance with the UV-vis spectral changes and indicative of the formation of intermediate **4**. For analyzing the changes in the mass spectrum, it is important to know that the  $\mu$ -oxodiiron(III) species **3** is not stable under ESI conditions and dissociates into **1** and **2**. Therefore, the ESI mass spectrum of the final product **3** (brown) shows peaks for its fragments  $[\text{L}^{\text{NHC}}\text{Fe}]^{2+}$  and  $[\text{L}^{\text{NHC}}\text{Fe}(\text{O})]^{2+}$ , the former giving rise to the emerging peak at  $m/z = 202.1$  (Figure 2, left).

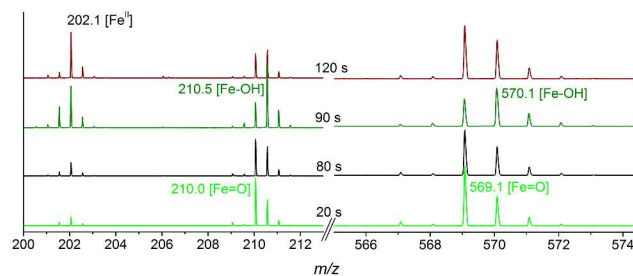


**Figure 2.** Part of the cryo-ESI mass spectrum of **1** (0.25 mM) during the reaction with CHD (25 mM); peak assignments:  $[\text{L}^{\text{NHC}}\text{Fe}^{\text{II}}]^{2+}$  at  $m/z = 202.1$ ,  $[\text{L}^{\text{NHC}}\text{Fe}^{\text{IV}}(\text{O})]^{2+}$  at 210.0,  $[\text{L}^{\text{NHC}}\text{Fe}^{\text{III}}(\text{OH})]^{2+}$  at 210.5,  $[\text{L}^{\text{NHC}}\text{Fe}^{\text{IV}}\text{O}(\text{OTf})]^{+}$  at 569.1 and  $[\text{L}^{\text{NHC}}\text{Fe}^{\text{III}}(\text{OH})(\text{OTf})]^{+}$  at 570.1. Peaks for the hydroxo-iron(III) species **4** reach their maximum after around 100 s.

In the present case, deriving kinetic data from the UV-vis spectral changes proved quite challenging. The most common strategy reported in literature is to monitor the decay of the active ferryl species upon addition of different amounts of substrates. However, this is not a suitable approach for **1**, because the final decay species (i.e.,  $\mu$ -oxo complex **3**) has optical features in the same region as **1**. However, the rather unusual observation of two well separated sequential processes in the UV-vis spectra for these C-H bond activation reactions allowed to focus on this first step only. It was thus decided to follow the kinetics of the absorbance at 448 nm which corresponds to the formation of the  $\text{Fe}^{\text{III}}(\text{OH})$  intermediate (**4**). This band shows a marked change in intensity reflecting the formation and subsequent decay of **4** (see inset of Figure 1), leading to consistent kinetic results for all sets of experiments, both with different concentrations of  $\text{Fe}^{\text{IV}}(\text{O})$  complex **1** and of the substrates. As mentioned above, under the applied reaction conditions, self-decay of **1** to **3** is negligible on the experimental time scale. Thus, it is assumed that the decay of **1** is caused exclusively by reaction with the added substrate via H-atom transfer (HAT) to form  $\text{Fe}^{\text{III}}(\text{OH})$  intermediate **4** (increase of the absorbance at 448 nm). Therefore, the  $k_{\text{obs}}$  derived from fitting the absorption trace to a single exponential can be considered as the absolute value  $k_{\text{obs}}$  for the decrease of the active ferryl complex **1**. Experiments at variable concentrations of **1** with a constant concentration of CHD (60 eq) showed  $k_{\text{obs}}$  to be independent of the concentrations of **1**, confirming that this process follows pseudo first order kinetics, and that we are dealing with a bimolecular reaction (Figure S1).

As depicted in Figure 3 (left), the plot of  $k_{\text{obs}}$  values versus different concentrations of substrate gave linear correlations. Consequently, the observed  $\log(k_2')$  of conversion for each substrate ( $k_2'$  is the second order rate constant  $k_2$  divided by the number of equivalent C-H bonds on the substrate; for values see Table S1) were plotted versus the bond dissociation energy (BDE) of the weakest C-H-bonds (Figure 3, right).<sup>19</sup> This correlation gives a relatively good linear fit with a slope of  $-0.39$ , which resembles the value obtained for previously reported oxo-iron(IV) complexes.<sup>3b,3c,20,21</sup> This finding supports the notion that the process of C-H bond activation by **1** occurs via an HAT mechanism and is sensitive to the BDE according to a Bell-Evans-Polanyi (BEP)<sup>22</sup> like correlation. No reactivity of **1** was observed towards substrates with stronger C-H bonds such as 2,3-dimethylbutane (BDE = 84 kcal mol<sup>-1</sup>) or cyclohexane (BDE = 99 kcal mol<sup>-1</sup>).

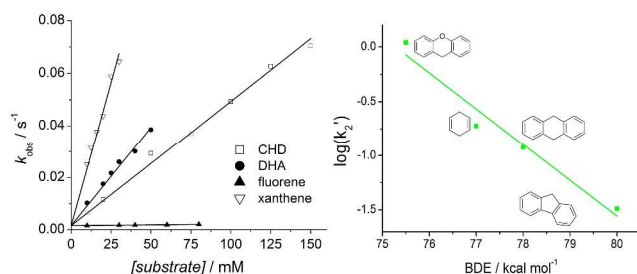


**Figure 3.** Left: Kinetic data for **1** with various substrates at 233 K in MeCN. Right: Plot of  $\log(k_2)$  against the weakest C–H BDE of different substrates for **1**.

To gain more insight into the mechanism of this process, deuterated dihydroanthracene (DHA- $d_4$ ) was used to study the kinetic isotope effect (KIE). As shown in Figure S2, the reaction with the deuterio substrate is much slower than for the protio substrate, leading to  $k_H/k_D = 32 \pm 8$  at  $-40^\circ\text{C}$ .<sup>23</sup> This markedly high value is close to the range reported for enzymes such as TauD and non-heme iron compounds reacting with ethylbenzene, whereas pMMO and most of the cyclam-coordinated iron complexes show lower KIE's (10-20).<sup>20,24,25</sup> However, all these unusual high values are suggestive of non-classical hydrogen tunneling effects<sup>20,7b</sup> and are consistent with HAT as RDS. Importantly, the large KIE for **1** is in agreement with reactivity occurring along an  $S = 1$  pathway, though it decreases with increasing temperature as previously observed for other systems, from KIE = 32 at  $-40^\circ\text{C}$  to 18 at  $-20^\circ\text{C}$  and 11 at  $0^\circ\text{C}$  (see Table S2). Extrapolating the experimental data, only a small a KIE ( $\sim 5$ ) is expected at  $20^\circ\text{C}$ , in agreement with the similar free energy of activation at this temperature (vide infra, Table 1). The temperature dependence reflects the decreasing influence of the differences in activation enthalpy for C–H and C–D with increasing temperature while the changes in entropy become more relevant. Tunneling contributions, which are barely affected by temperature, may complicate these trends in KIE as has been pointed out in literature.<sup>10,26</sup>

Additionally, we studied the reaction products resulting from the oxidation of DHA by **1**. As described in literature, under stoichiometric conditions a non-rebound HAT process leads to a maximum formation of 0.5 eq. of anthracene per 1 eq. of  $\text{Fe}^{\text{IV}}(\text{O})$  complex, as two H-atoms need to be abstracted.<sup>27</sup> In our case, the yield was determined to be already 0.32 eq. of anthracene (64% of the theoretical maximum yield) when the maximum in absorbance at 448 nm was reached after around 100 s, and 0.37 eq. (74%) after 1 h. Consequently, the major amount of anthracene (87% of the final yield) is already generated during the initial process which is in line with the proposed formation of a  $\text{Fe}^{\text{III}}(\text{OH})$  intermediate in that first reaction step. Notably, anthracene was the only observed product indicating that after the initial HAT no radical rebound that might lead to any oxygenated product occurs.<sup>28</sup> In this context it is interesting to note that oxygen atom transfer reactivity of **1** is essentially lacking. In fact, no significant reactivity of  $\text{Fe}^{\text{IV}}(\text{O})$  complex **1** toward common substrates such as MeSPh or  $\text{PPh}_3$  was observed. This effect might be due to the high basicity of the tetracarbene oxoiron(IV) system that allows for moderate HAT reactivity while the 2-electron OAT process is not influenced by  $\text{p}K_a$  but is correlated with the redox potential only (vide infra).<sup>29</sup>

The reaction of **1** with 20 eq. of CHD, DHA and DHA- $d_4$  was performed in the temperature range between  $-40^\circ\text{C}$  and  $0^\circ\text{C}$ , and the experimentally determined  $k_2$  values were used to derive activation parameters from an Eyring analysis. Plotting  $\ln(k_2/T)$  versus  $1/T$  (Figures S3 and S4) gives good linear fits with  $\Delta H^\ddagger = 8.5$  kcal/mol and  $\Delta S^\ddagger = -22.9$  cal/Kmol for CHD and  $\Delta H^\ddagger = 8.5$  kcal/mol and  $\Delta S^\ddagger = -22.4$  cal/Kmol for DHA, respectively (Table 1). Thus, the obtained activation parameters for the reaction of **1** with both substrates are very similar, in agreement with the similar BDE. In accordance with the higher BDE for a C–D bond, a significantly higher activation enthalpy (13.0 kcal/mol, Figure S5) was determined for the deuterated substrate. Surprisingly, C–H/C–D exchange is also accompanied by a decrease in entropy of activation. This effect might be due to enthalpy/entropy compensation as observed for intermolecular interactions involving hydrogen bonds.<sup>30</sup>

**Table 1.** Thermodynamic parameters of the reaction of **1** with CHD, DHA and DHA- $d_4$  derived from an Eyring Plot.

	<b>1</b> with CHD	<b>1</b> with DHA	<b>1</b> with DHA- $d_4$
$\Delta H^\ddagger$ / kcal/mol	$8.5 \pm 0.2$	$8.5 \pm 0.2$	$13.0 \pm 0.5$
$\Delta S^\ddagger$ / cal/K mol	$-22.9 \pm 0.8$	$-22.4 \pm 0.7$	$-11.6 \pm 2.0$
$\Delta G^\ddagger_{20^\circ\text{C}}$ / kcal/mol	$15.2 \pm 0.9$	$15.1 \pm 0.8$	$16.4 \pm 1.1$

**Table 2.** Comparison of kinetic parameters of **1** and **A**.<sup>3a</sup> All reactions were performed at  $-40^\circ\text{C}$  in MeCN.

	<b>1</b>	<b>A</b> <sup>3a</sup>
$k_2(\text{xanthene})$	2.2	$6.6 \cdot 10^{-2}$
$k_2(\text{DHA})$	0.76	$2.5 \cdot 10^{-3}$
$k_2(\text{CHD})$	0.48	$6.4 \cdot 10^{-4}$
$k_2(\text{fluorene})$	$6.4 \cdot 10^{-3}$	$3.2 \cdot 10^{-5}$

**Reactivity comparison between **1** and **A**.** The experimentally obtained bimolecular reaction rates allowed a direct comparison with the literature reported values for complex **A** under identical conditions (MeCN,  $-40^\circ\text{C}$ ).<sup>3a</sup> Rate constants presented in Table 2 clearly show that **1** features significantly higher HAT reactivity than **A** by about two to three orders of magnitude depending on the substrate. Comparison with other literature known  $\text{Fe}^{\text{IV}}(\text{O})$  compounds classifies **A** to have rather low and **1** to have intermediate reactivity.<sup>18</sup> The so far most reactive oxo-iron(IV) complexes do not only show reaction rates up to four orders of magnitude higher than **1** but also the ability to activate substrates with stronger C–H bonds such as cyclohexane (BDE = 99 kcal/mol).<sup>7b,31</sup> Numerous reports have demonstrated the crucial influence of the supporting ligands on the oxidation and oxygenation reactivity of oxo-iron(IV) complexes.<sup>2,3</sup> For macrocyclic tetradentate scaffolds, variations such as different axial coligands or different macrocyclic ring sizes can significantly increase or decrease the reaction rate. For example, the oxo-iron(IV) unit coordinated by 13-TMC (13-TMC = 1,4,7,10-tetramethyl-1,4,7,10-tetraazacyclo-tridecane) – a macrocyclic ligand system smaller by one  $\text{CH}_2$  group compared to 14-TMC – is about  $3 \cdot 10^3$  times more reactive than **A**.<sup>3a</sup> Having this in mind, it is not surprising that **1** and **A** show different reactivity in C–H bond activation due to their differences in the supporting ligand system.

Important parameters that determine the driving force of HAT processes by oxo-iron(IV) species are the

iron(III)/iron(IV) redox potential as well as the basicity of the Fe(O) unit.<sup>32</sup> The interplay of both factors determines the ground state energy and thus the thermodynamics of the PCET process, for which HAT can be viewed as a special case where the proton and electron involved originate from the same source, viz. the C-H bond being cleaved. Unfortunately, so far it was not possible to determine the  $pK_a$  value or an exact value for  $E^0$  for the tetracarbene-coordinated system discussed herein. As mentioned above, because of the negligible OAT reactivity we assume that the  $pK_a$  of **1** might be rather high while the Fe<sup>III</sup>/Fe<sup>IV</sup> redox potential is relatively low. Hence the discussion will be focused on the kinetics and activation energies of these HAT reactions. The key distinction when comparing the tetracarbene coordinated system **1** with **A** is that the electronic structure of **1** differs fundamentally from those of all previously reported tetragonal oxo-iron(IV) complexes with equatorial N-donor ligands.<sup>2</sup> Because of the extremely strong  $\sigma$ -donating carbenes in **1**, its  $d_{x^2-y^2}$  orbital is lifted in energy resulting in a reversed energetic order of the high lying  $d_{x^2-y^2}$  and  $d_{z^2}$  orbitals and in a much larger HOMO-LUMO gap, which was anticipated to have a decisive effect of the potential involvement of the  $S = 1$  and  $S = 2$  reactive spin states.

**Calculations.** To evaluate the reactivity differences of complexes **1** and **A** and to gain deep insights into their reaction mechanisms, we have carried out detailed computational studies on their HAT processes. For transition metal complexes, DFT calculations often fail to provide a reliable and systematic accuracy in predicting relative energies that can vary up to 10 kcal/mol with different choice of exchange-correlation functionals.<sup>33</sup> A recent benchmark study showed that among a variety of density functionals B3LYP delivers the most accurate energy profile for H<sub>2</sub> activation by (FeO)<sup>+</sup>.<sup>34</sup> In addition to B3LYP, complete active space self-consistent field (CASSCF)<sup>35</sup> followed by  $N$ -electron valence perturbation theory up to second order (NEVPT2)<sup>36</sup>, a wavefunction based multireference approach, has been used to calculate the accurate energies of the critical points on the potential-energy surfaces (PESs).

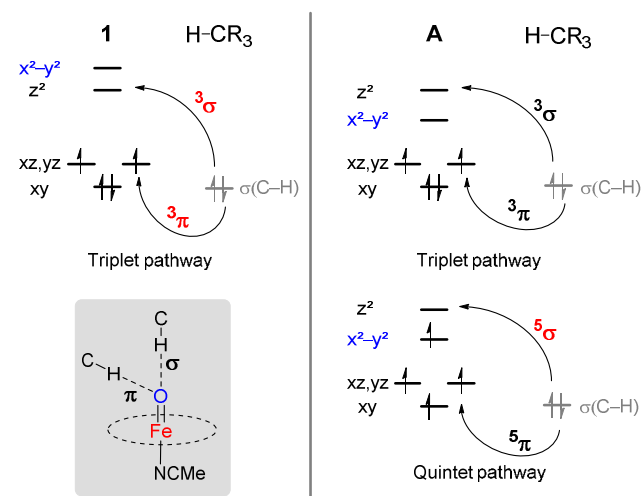
As elaborated above, the relative energies of the triplet and quintet states for complexes **1** and **A** are crucial for their reactivity. To compute reliable quintet-triplet energy separations ( $\Delta E_{Q-T}$ ), we have considered three different active spaces. Our earlier work showed that a minimum balanced active space should consist of 12 electrons in 9 orbitals (CAS(12,9)), viz. the five iron 3d based orbitals, the three oxygen  $p$ -orbitals, and the bonding counterpart of the Fe- $d_{x^2-y^2}$  orbital.<sup>14,37</sup> On top of CAS(12,9), we added the iron 4d and 3p shells into the active space, leading to CAS(12,14) and CAS(18,12), respectively. The former active space accounts for the double-shell effect, which considerably affects the spin-state energetics of transition metal complexes, as extensively documented in the literature.<sup>38</sup> Recently, Pierloot and coworkers proposed that the core-correlation might also have appreciable influence on the spin-state energetics,<sup>39</sup> for which the latter active space was designed.

The CASSCF(12,9)/NEVPT2 calculations estimate rather large quintet-triplet energy differences for both complexes (complex **1**,  $\Delta E_{Q-T} = 30.4$  kcal/mol, complex **A**,  $\Delta E_{Q-T} = 14.9$  kcal/mol). Inclusion of the second  $d$ -shell changes the  $\Delta E_{Q-T}$  values by  $\sim 5$  kcal/mol (complex **1**,  $\Delta E_{Q-T} = 34.9$  kcal/mol; complex **A**,  $\Delta E_{Q-T} = 8.6$  kcal/mol), and the core-correlation effect lowers the energy gaps to 28.7 and 5.0 kcal/mol for

complexes **1** and **A**, respectively. Thus, one can anticipate that more accurate values can be obtained by the calculations including both iron 4d and 3p shells into the active space, which likely covers most of the important electron-correlations. However, the resulting active space CAS(18,17) becomes too large to be handled by usual configuration interaction procedures. Our earlier B3LYP calculations<sup>14</sup> predicted that the triplet ground state of complex **1** is energetically well separated from the lowest-energy quintet state by 18.6 kcal/mol, whereas a vanishingly small quintet-triplet gap of  $\sim 2$  kcal/mol is found for complex **A**. Taken together, our theoretical results unanimously suggest that the quintet state of complex **1** is thermally inaccessible; hence, the HAT process can only occur on the triplet surface. While in the case of complex **A** the marginal quintet-triplet energy gap permits an easy access to the quintet surface; thus, for **A** the HAT reaction may take place on the triplet and quintet surfaces.

For HAT processes performed by classical ferryl models such as complex **A**, the feasible electron accepting orbitals (EAOs) are found to be  $d_{xz/yz}$  and  $d_{z^2}$ , whereas  $d_{xy}$  and  $d_{x^2-y^2}$  function as inspectors because the latter two orbitals cannot interact with the target C-H  $\sigma$ -bond.<sup>40</sup> As such, an oxo-iron(IV) species with a given spin multiplicity can employ two channels to activate C-H bonds, of which one is referred to as the  $\pi$ -trajectory with the  $d_{xz/yz}$  orbitals serving as the EAO and the other involving the  $d_{z^2}$  orbital is termed  $\sigma$ -route. Therefore, there are in total four viable pathways for the reaction with complex **A**, as depicted in the right panel of Scheme 3.<sup>40a,41</sup> On the other hand, one can envision that only two triplet-channels can be adopted by complex **1** owing to the unavailability of the quintet state (Scheme 3, left panel).

**Scheme 3. Possible substrate attack trajectories and electron transfer pathways for the HAT processes mediated by complex **1** and **A**. Highlighted in red are the most favorable pathways. The inset depicts the optimal attack geometry of the substrates for the  $\sigma$  and  $\pi$  pathways.**



We succeeded in locating the two relevant triplet TSs for complex **1** by using B3LYP (the nature of the TSs ( $\sigma$  vs.  $\pi$ ) will be verified below.), in addition to the four pathways for complex **A**. To compute reliable barriers at the CASSCF/NEVPT2 level of theory, we made very careful

selection of active spaces in order to properly describe breaking C-H and forming O-H bonds. During the reaction the change in the metal oxidation state induces substantial adjustments of the radial electron correlation.<sup>42</sup> It has been shown that to account for this effect the active space needs to include metal double d-shells;<sup>43</sup> hence, we have to add key Fe 4d orbitals instead of Fe 3p orbitals in the active space. Eventually, an active space of CAS(14,14) for the TSs is required. A detailed description of the active space construction is documented in the experimental section. The CASSCF/NEVPT2 energy profiles are presented in Figure 4, which, to the best of our knowledge, is the first HAT PES constructed by multi-reference calculations. For the TSs and intermediates (Is), we have used shorthand notations  ${}^m\mathbf{X}_n$ , where  $\mathbf{X}$  represents either **TS** or **I**, and  $m$  and  $n$  are the spin multiplicity (triplet or quintet) and the type of TS ( $\sigma$  or  $\pi$ ), respectively. The free energy difference between the reaction complex (**RC**) and the separated reactants (**1** or **A** + **CHD**) is largely dictated by an unfavorable entropy term for a combination reaction, which is partly compensated by weak non-covalent interactions. Such effects mainly originate from dynamic electron correlation that cannot be appropriately treated by the CASSCF approach, which is designed to cover most of the static electron correlation. In this regards, DFT calculations in combination with explicit non-covalent corrections are expected to deliver reliable results.<sup>44</sup> Hence, we did not calculate this energy gap by using CASSCF.

Our CASSCF(14,14)/NEVPT2 results for complex **1** reveal that the  $\sigma$ -pathway ( ${}^3\mathbf{TS}_\sigma$ ) is more favorable than the  $\pi$ -route ( ${}^3\mathbf{TS}_\pi$ ) by  $\sim 4$  kcal/mol (Figure 4a, upper panel), whereas a barrier difference of  $\sim 2$  kcal/mol, falling within the well-established DFT error range ( $\sim 3$  kcal/mol),<sup>45</sup> is estimated by the B3LYP calculations (Figure 4a, lower panel). Despite this subtle difference, the barriers calculated by the two theoretical approaches are considerably lower than the corresponding quintet-triplet gaps, thereby corroborating the notion that the reaction with complex **1** indeed exhibits pure triplet-state reactivity. A recent DFT study on a related tetracarbenic ferryl

complex (having a smaller tetra-NHC macrocycle with four methylene bridges)<sup>46</sup> suggests that the *trans* coordination of MeCN slows down the reaction.<sup>47</sup> We carefully examined this hypothesis for complex **1**. In fact, the Fe–NCMe bonding in **1** is rather weak, because the dissociation of MeCN from the Fe center is computed to be almost thermoneutral (Figure S8). The optimized geometry of  ${}^3\mathbf{TS}_\sigma$  shows that the Fe–NCMe bond is completely broken with the Fe–NCMe distance of 3.929 Å (vs. 2.438 Å in  ${}^3\mathbf{RC}$ ). Therefore, five-coordinate complex **1'** may take part in the actual HAT process. Similar to complex **1**, complex **1'** with a large quintet-triplet separation of 15.6 kcal/mol (CASSCF/NEVPT2 value) also features single-state reactivity (Figure 4b). We found that the CASSCF(14,14) calculations on the B3LYP-optimized geometry of  ${}^3\mathbf{TS}_\pi$  always converge to a dominant electron configuration analogous to  ${}^3\mathbf{TS}_\sigma$ , thus indicating that  ${}^3\mathbf{TS}_\pi$  is situated at a much higher energy than  ${}^3\mathbf{TS}_\sigma$ . In comparison with complex **1**, our theoretical results predict enhanced reactivity of complex **1'**. This could be readily attributed to the diminished energetic penalty required to promote an electron from the  $\sigma_{\text{C-H}}$  bond, the EDO of HAT, to the stabilized Fe- $d_{z^2}$  orbital (EAO) in complex **1'**.<sup>48</sup> The overall HAT barrier for complex **1'** is 15.1 and 15.7 kcal/mol delivered by the CASSCF/NEVPT2 and B3LYP computations, respectively (Figures 4b). The corresponding values for complex **1** are 18.1 and 18.5 kcal/mol.

Given the uncertainty of our calculations, the computed barriers are in reasonable agreement with the activation parameters determined experimentally ( $\Delta G^\ddagger_{20^\circ\text{C}} = 15.2 \pm 0.9$  kcal/mol), especially for complex **1'**. In addition to CHD, we also calculated the HAT reactivity of complex **1** toward DHA (Figure S9). Our DFT results show that both reactions involve similar barriers of  $\sim 19$  kcal/mol owing to their nearly identical C–H bond dissociation energies (CHD: 78 kcal/mol; DHA: 77 kcal/mol<sup>19</sup>).

### CASSCF/NEVPT2

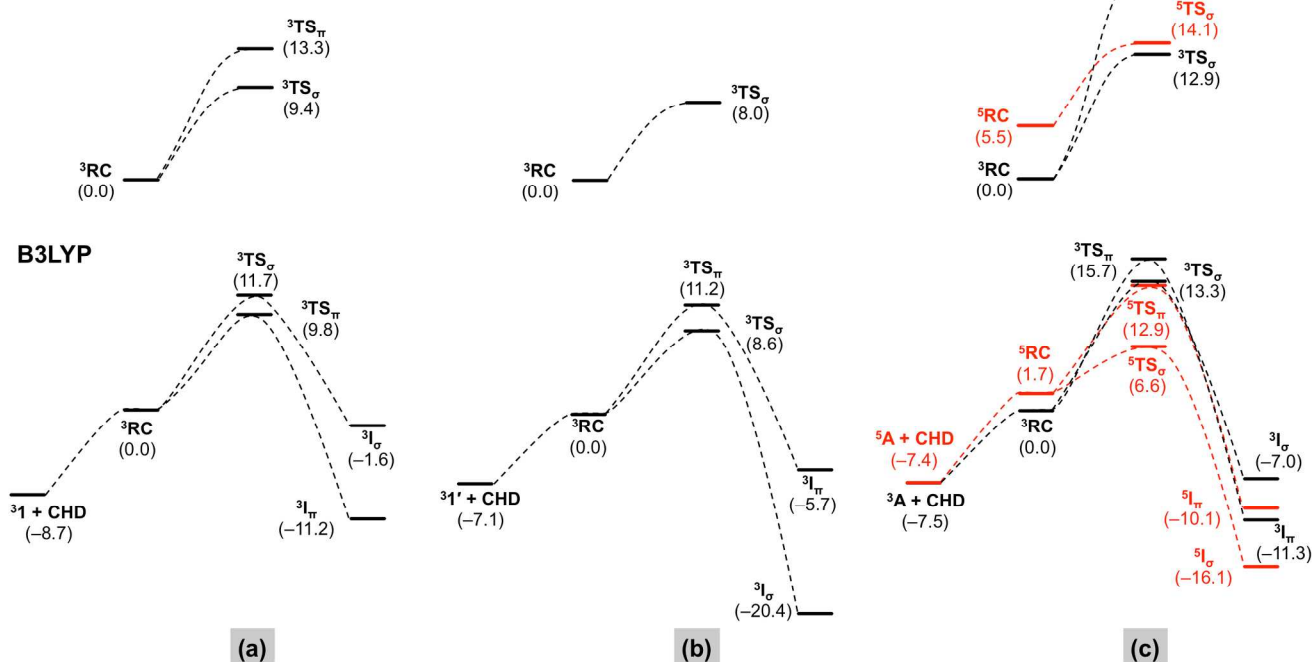


**Figure 4.** Computed free energy ( $\Delta G$ ) profiles of the HAT processes from CHD for (a) complex **1** (b) complex **1'** (c) complex **A**. The CASSCF/NEVPT2 profile is presented in the upper panel and the B3LYP profile is presented in the lower panel. Black line: triplet pathways; Red lines: quintet pathways.

In case of complex **A**, our CASSCF/NEVPT2 results demonstrate that the quintet  $\sigma$ -pathway has the lowest barrier (8.6 kcal/mol) and hence is the most efficient reaction channel to accomplish HAT (Figure 4c), while the triplet channels need to traverse barriers at least 4 kcal/mol higher. For  ${}^5\text{TS}_\pi$ , our CASSCF(14,14) computations couldn't converge to the correct electronic state, but to one corresponding to  ${}^5\text{TS}_\sigma$ , an analogous situation found for  ${}^3\text{TS}_\pi$  of complex **1'**. The CASPT2 (multireference perturbation theory up to second order based on CASSCF wavefunction)<sup>49</sup> calculations on a model oxo-iron(IV) system (the oxo-iron(IV) site in magnesium-diluted  $\text{Fe}_2(\text{dobdc})$  metal-organic framework;  $\text{dobdc} = 2,5$ -dioxo-1,4-benzenedicarboxylate) suggest that  ${}^5\text{TS}_\sigma$  is stabilized by 5.8 kcal/mol relative to  ${}^5\text{TS}_\pi$ .<sup>50</sup> The barrier for the quintet  $\sigma$ -pathway estimated by B3LYP is 4.9 kcal/mol, and the closest triplet  $\sigma$ -channel is  $\sim 7$  kcal/mol higher in energy, both values comparable to those reported by Siegbahn and coworkers.<sup>51</sup> In comparison with the CASSCF/NEVPT2 results, B3LYP considerably underestimate the  ${}^5\text{TS}_\sigma$  barrier, which has been observed in an earlier computational study<sup>51</sup> on the reactivity of complex **A** and attributed to the self-interaction error<sup>52</sup> of DFT calculations. Furthermore, to more accurately evaluate the reactivity of complex **A**, we located the minimum-energy crossing point (MECP) between its triplet and quintet surfaces, which can be regarded as the upper bound of the corresponding spin-crossover barrier. It turns out that the MECP is situated only 1.5 kcal/mol above  ${}^3\text{RC}$ , falling within the barrier range of 1–4 kcal/mol calculated for similar spin-crossover processes.<sup>53</sup> The optimized geometries of  ${}^5\text{TS}_\sigma$  and  ${}^3\text{TS}_\sigma$  for complex **A** show that the axial Fe–N bonds are only slightly lengthened by 0.09 and 0.26 Å, respectively. Thus, dissociation of the *trans* axial ligand is unlikely to happen for complex **A**, different from complex **1**. Considering the inadequacy of the employed active space in predicting

reliable spin-state energetics (*vide supra*), our CASSCF/NEVPT2 calculations on complex **A** may somewhat overestimate the relative energy of  ${}^5\text{RC}$  relative to  ${}^3\text{RC}$ . However, by neglecting the energy gap between  ${}^5\text{RC}$  and  ${}^3\text{RC}$  and the spin-crossover barrier, we can estimate the lowest limit of the HAT barrier for complex **A**. The value of 16.1 kcal/mol thus obtained is similar to the lowest barriers found for complexes **1** and **1'**. Our CASSCF/NEVPT2 calculations thus indicate that complex **1** is likely to be slightly more reactive than complex **A**, consistent with the observed two to three orders of magnitude difference in their reaction rates, which translates into a reaction-barrier separation of only 2–4 kcal/mol. In contrast to this, DFT calculations predict competitive reactivity for the two systems within the uncertainties of DFT methods ( $\sim 3$  kcal/mol). This lends credence to our employed CASSCF/NEVPT2 method and showcases the importance of multireference calculations for oxo-iron(IV) systems. As elaborated below, although complex **1** features a distinct electronic structure, its HAT reaction follows the same mechanism as the triplet state HAT of complex **A**. As such, our theoretical results show that complex **1**, while exhibiting single-state-reactivity, can activate C–H bonds at least with paralleled efficiency to complex **A**, which features two-state-reactivity.

**Electronic-structure analysis.** To gain more mechanistic insights about complex **1**, we carried out a detailed analysis by mapping the electronic-structure changes along the reaction coordinate. Oxo-iron(IV) complexes feature rather covalent iron-oxo interactions, consisting of two  $\pi$ -bonds involving the Fe- $d_{xz/yz}$  and O- $p_{xy}$  atomic orbitals and one  $\sigma$ -bond formed by Fe- $d_z$  and O- $p_z$ .<sup>40a,16,54</sup> To properly describe such covalent interactions, a balanced active space has to include not only metal-centered antibonding orbitals but also the corresponding bonding orbitals.<sup>43</sup>

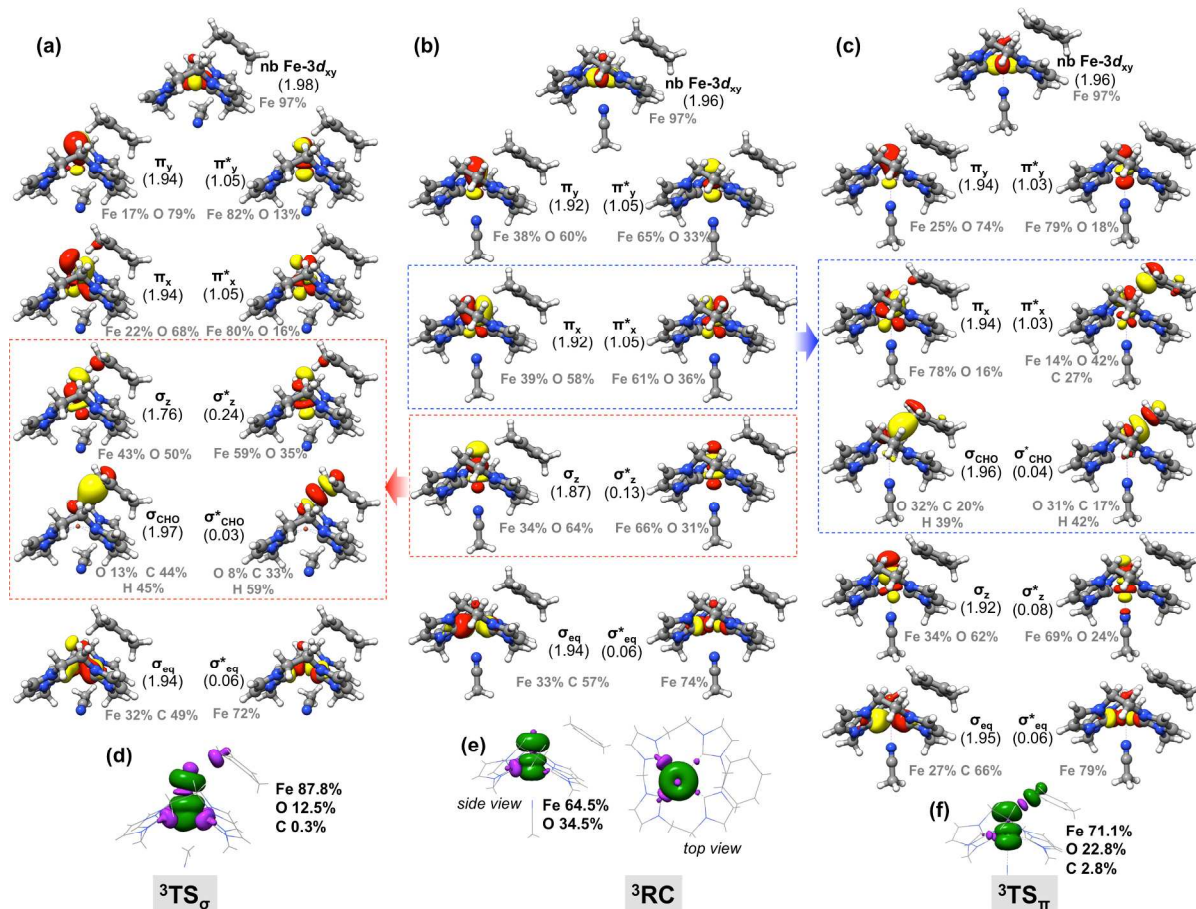


**Figure 5.** Comparison of the electronic structures of the reactant complex (RC) and transition states (TS) involved in the HAT processes by complex 1 and CHD. (a), (b), and (c) represents CASSCF natural orbitals along with the occupation numbers in parenthesis below the orbital labels and atomic contributions for  ${}^3\text{TS}_\sigma$ ,  ${}^3\text{RC}$  and  ${}^3\text{TS}_\pi$ , respectively; (d), (e), and (f) represents CASSCF spin-density for  ${}^3\text{TS}_\sigma$ ,  ${}^3\text{RC}$  and  ${}^3\text{TS}_\pi$ , respectively. (green: positive density; magenta: negative density)

As shown in Figure 5b, the occupation numbers (ONs) of most valence orbitals are markedly greater than 0.02 and lower than 1.98, in CASSCF calculations a virtual molecular orbital (VMO) typically having an ON of no more than 0.02 and a doubly occupied molecular orbital (DOMO) having an ON of no less than 1.98. This observation clearly indicates significant multireference character in complex 1, and the results delivered by single-determinant DFT approaches hence need be viewed with caution. The sum of the ONs of the bonding and antibonding orbitals is close to that expected for an electron configuration of  $(\sigma_{\text{eq}})^2(\sigma_z)^2(\pi_{x/y})^4(\text{nb } d_{xy})^2(\pi_{x/y}^*)^2(\sigma_{\text{eq}}^*)^0(\sigma_z^*)^0$  (eq = equatorial, nb = non-bonding). The computed spin-density plot of complex 1 demonstrates that the oxo group has large donut-like positive spin density in the xy-plane and small yet discernable negative spin density in the z-direction (Figure 5e, top-view). Due to the covalent iron-oxo bonding, the singly occupied molecular orbitals (SOMOs) mainly with the Fe- $d_{xz/yz}$  parentage contain substantial contributions from the O- $p_{x/y}$  atomic orbitals (~30%), thereby resulting in sizeable positive spin density on the oxo ligand. Because the Fe center has a much larger spin population than the oxo ligand, the exchange stabilization induces some positive spin density in the Fe- $d_{z^2}$  orbital and accordingly some negative spin density in the O- $p_z$  orbital, a spin-polarization process taking place. This analysis explains why the ON of the O- $p_z$  based  $\sigma_z$  orbital, a formal DOMO, considerably deviates from two (1.87), and the

ON of the antibonding  $\sigma_z^*$  orbital with the predominant Fe- $d_{z^2}$  character, a formal VMO, appreciably differs from zero (0.13).

In the HAT TSS, the target C-H is partially broken. Following the same line of the reasoning about how to construct a balanced active space, we need to include the  $\sigma_{\text{C-H}}$  and  $\sigma_{\text{C-H}}^*$  orbitals into the active space. The spin-density plot of  ${}^3\text{TS}_\sigma$  shows that some negative spin density develops in the substrate, indicative of a  $\sigma$  TS (Figure 5d). In comparison with complex 1, no substantial changes in the ONs of all valence orbitals were found except  $\sigma_z$  and  $\sigma_z^*$  (Figure 5a). Surprisingly, the ON of  $\sigma_z^*$  rises at the expense of that of  $\sigma_z$ , and consequently the sum of the ONs for both orbitals remain two. Thus, the deviations of the ONs from their ideal numbers for a DOMO and a VMO become more pronounced in  ${}^3\text{TS}_\sigma$ . This change signals the onset of homolytic cleavage of the iron-oxo  $\sigma$ -bond, similar to  $\text{H}_2$  homolysis. At the equilibrium geometry of  $\text{H}_2$ , one can anticipate that the ON of the  $\sigma_{\text{H-H}}$  orbital should be two, and that of  $\sigma_{\text{H-H}}^*$  should be zero. As the H-H bond lengthens, the ON of  $\sigma_{\text{H-H}}$  decreases and simultaneously that of  $\sigma_{\text{H-H}}^*$  increases. Eventually, both values are close to one when the two hydrogen atoms are farther apart. This interpretation rationalizes the much larger negative spin density in the O- $p_z$  orbital found for  ${}^3\text{TS}_\sigma$  compared to complex 1. Therefore, our multireference calculations suggest that during the reaction a transient oxyl radical ( $\text{O}^\cdot$ ) forms, the same conversion found in the quintet  $\sigma$ -pathway of HAT by classi-

cal ferryl complexes.<sup>40c,55</sup> Originally in complex **1** the  $\pi_x$  orbital is  $O-p_x$  based; during the reaction this orbital acquires substantial  $Fe-d_{xz}$  character and has dominant  $Fe-d_{xz}$  parentage in  ${}^3TS_\pi$ , this observation pointing to a transformation from oxo-iron(IV) to oxyl-iron(III) ( $Fe^{III}-O^\cdot$ ). By analyzing the lead electron configurations of the CASSCF wave functions of  ${}^3TS_\sigma$  and  ${}^3TS_\pi$ , one can reach the same conclusion (for details, see the supporting information, Tables S3,S4).<sup>50</sup> The resulting oxyl radical interacts with the EDO, leading to formation of a pair of three-center orbitals, viz.  $\sigma_{CHO}$  and  $\sigma_{CHO}^*$ , and the former orbital evolves to  $\sigma_{O-H}$  in hydroxyl-iron(III) and the latter to a C-radical, reminiscent of an organic radical, such as  $OH^\cdot$ , abstracting an H-atom from alkanes.<sup>54</sup> Thus, the C–H bond activation by ferryl intermediates can be essentially viewed as a radical reaction, but at the early phase of the reaction the oxyl radical is masked by the covalent iron-oxo interaction.<sup>56</sup> Apparently, the reaction involves rather sophisticated electronic-structure changes, for which the electron shift diagram depicted in Scheme 3 only gives a phenomenological picture of it. In comparison with the HAT processes mediated by classical ferryl species,<sup>51,57</sup> the reactive  $Fe^{IV}(O)$  unit in complex **1** undergoes the same electronic-structure adjustments. Therefore, the reactivity of complex **1**, while featuring a distinct electronic configuration, represents the intrinsic triplet HAT efficacy of ferryl intermediates.

## CONCLUSIONS

The organometallic  $S = 1$  oxo-iron(IV) complex  $[L^{NHC}Fe^{IV}(O)(MeCN)]^{2+}$  (**1**), while topologically related to other tetragonal oxo-iron(IV) complexes such as the standard system  $[L^{TMC}Fe^{IV}(O)(MeCN)]^{2+}$  (**A**), features a unique electronic structure, as evidenced recently by an extensive MCD study.<sup>14</sup> The strongly  $\sigma$ -donating equatorial tetracarbene ligand in **1** does not affect the bonding within the  $Fe^{IV}(O)$  unit but strongly destabilizes the  $d_{x^2-y^2}$  orbital, which leads to a very large energetic triplet-quintet splitting and presumably prohibits any spin crossover to the high-lying  $S = 2$  state. To assess the electronic structure impact on the reactivity, we have here presented experimental results for the C–H activation reactions of **1** with a set of substrates featuring C-H BDEs ranging from 75 to 80 kcal/mol. BEP-like correlation of second order rate constants  $k'_2$  with BDEs supports the notion that the process of C–H bond activation by **1** occurs via a HAT mechanism, and the putative hydroxo-iron(III) HAT intermediate has been detected by cryo-ESI mass spectrometry. No reaction occurs with substrates having stronger C-H bonds, and also no significant OAT reactivity of **1** is observed. Kinetic parameters for the HAT process and comparison with the large body of known oxo-iron(IV) complexes shows that the reactivity of **1** is moderate, but significantly higher than the reactivity of related standard compound **A** that was proposed to follow a TSR pathway under the same experimental conditions; second order rate constants  $k'_2$  are two to three orders of magnitude higher in case of **1**. The very large KIE observed for **1** is in agreement with  $S = 1$  being the reactive spin state. CASSCF/NEVPT2 and DFT calculations confirmed that for **1** the reactions with C-H substrates such as CHD and DHA take place on the triplet surface only, because the computed HAT barrier on the triplet surface is substantially lower than the triplet-quintet energy separation. The theoretical results delivered by the CASSCF/NEVPT2 calculations nicely explain the observed reactivity difference between complexes **1** and **A**; however, DFT fails. To the best of our knowledge, this is the

first ab initio study on the reactivity of oxo-iron(IV) species. A detailed analysis reveals that in the course of HAT, the  $Fe^{IV}(O)$  core in complex **1** undergoes the same electronic-structure changes as those found for classical ferryl models such as **A**, i.e. for both systems the reactions follow an identical mechanism. As such, complex **1** is a trend-breaking example of an  $S = 1$  oxo-iron(IV) species that shows efficient reactivity confined to single-state pathways, and that now represents a pure ‘triplet-only’ model.

## EXPERIMENTAL SECTION

**General Considerations.** All reactions were carried out in UV/vis cuvettes prepared inside a glove box (MBRAUN LabMaster) under nitrogen atmosphere with less than 0.1 ppm  $O_2$  and  $H_2O$  and kept under a nitrogen atmosphere. Acetonitrile was dried and degassed by standard procedures before use. Soluble iodosobenzene, DHA- $d_4$  and compound **1** were prepared according to literature.<sup>58,20,12</sup> Other chemicals were purchased from commercial sources and used as received. Cryo Mass spectrometry was recorded using a high-resolution mass spectra (HR-MS) Bruker MicroTOF-Q IITM instrument using cryospray ionization sources using a cryospray attachment and setting the temperature of the nebulizing and drying gas at  $-40^\circ C$ .

UV-vis spectroscopy was performed using an Agilent 8453 UV-vis spectrophotometer. Absorption of 1 mM solutions of the complexes in acetonitrile was measured from 200 nm to 800 nm with a resolution of 1 nm in a 1 cm UV quartz cells. The low temperature control was performed with a cryostat from Unisoku Scientific Instruments (Japan). The GC measurement was performed by a Thermo Finnigan TRACE GC with EI and Varian GC Capillary Column.

**Formation of  $[Fe^{IV}O(L^{NHC})(MeCN)]^{2+}$  and reaction with substrates.** A 1 mM solution of  $[Fe^{II}(L^{NHC})(MeCN)_2]^{2+}(OTf)_2$  (1.569 mg, 2  $\mu$ mol) in acetonitrile (2 mL) was cooled to  $-40^\circ C$ . A precooled and freshly prepared solution of 2-(tBuSO<sub>2</sub>)-C<sub>6</sub>H<sub>4</sub>-IO (1.905 mg, 5.60  $\mu$ mol, 2.8 eq.) in  $CH_2Cl_2$  (190.5  $\mu$ L) was added and the cuvette was transferred out of the glove box and the UV/vis absorption measurement at  $-40^\circ C$  was started. The appropriate amount of substrate (10 – 160 eq) was dissolved in Acetonitrile (CHD) or  $CH_2Cl_2$  (DHA, Xanthene, Fluorene) to give 100  $\mu$ L (because of solubility problems sometimes up to 200  $\mu$ L) which were then added to the cuvette using a syringe. The subsequent increase of the characteristic absorption band of the iron(III)-hydroxo (448 nm) was directly monitored and fitted to a single exponential function.

Product analysis for the oxidation of DHA was performed by gas chromatography. Therefore, a 1 mM solution of crystalline material of **2** (2.21 mg, 2.91  $\mu$ mol) in acetonitrile (2.91 mL) was reacted with 10 eq of DHA (5.25 mg in 100  $\mu$ L  $CH_2Cl_2$ ) as described previously. The yield was determined after 3 min, which corresponds to maximum absorption at 448 nm, and after 1 h. Prior to injection, the solution was filtered through silica and washed with acetonitrile, ethyl acetate and dichloromethane. Anthracene was the only observed product and its amount was compared to leftover amount of DHA since both substances show very similar intensity in GC. After 3 min 0.93  $\mu$ mol (64% compared to the maximum theoretical yield) anthracene was detected, after 1 h 1.08  $\mu$ mol (74%).

**Computational Details.** All calculations were performed by using the ORCA program package.<sup>59</sup> Geometry optimiza-

tions were undertaken by employing the hybrid-GGA (GGA = generalized gradient approximation) density functional, B3LYP,<sup>60</sup> in conjunction with def2-TZVP(-f)<sup>61</sup> basis set without *f* polarization function for the first coordination sphere (Fe, O, N and C) and C and H participating in the reaction and def2-SVP<sup>62</sup> basis set for the rest of atoms. The scalar relativistic zeroth-order regular approximation (ZORA)<sup>63</sup> was applied in geometry optimizations as well as single point energy calculations. To speed up the overall calculations, the RIJCOSX approximation<sup>64</sup> was applied for the expensive integral calculations. To be consistent with the experiment, we carried out all calculations by applying the conductor-like polarizable continuum model (CPCM) with acetonitrile ( $\epsilon = 36.6$ ) being the solvent.<sup>65</sup> Non-covalent interactions, important for the reaction complexes and transition states, were accounted for by using atom-pairwise dispersion corrections with Becke-Johnson (D3BJ) damping.<sup>44</sup> Subsequent numerical frequency calculations were undertaken on the optimized geometries, which revealed stationary points featuring no imaginary frequency and first-order saddle points having one imaginary frequency. The zero-point vibrational energies, thermal corrections and entropy terms were obtained from the frequency calculations. Final single point energy calculations were undertaken by using the B3LYP functional in conjunction with a more flexible basis-set def2-TZVPP.<sup>66</sup>

Multiconfigurational calculations based on complete active space self-consistent field (CASSCF)<sup>35</sup> followed by *N*-electron valence perturbation theory up to second order (NEVPT2)<sup>36</sup> were performed in conjunction with def2-TZVPP<sup>66</sup> basis set. For the reaction complexes (RCs), we chose CAS(12,14) active-space consisting of five iron 3*d* based orbitals, the three oxygen *p*-orbitals, the bonding counterpart of the Fe-*d*<sub>x<sup>2</sup>-y<sup>2</sup></sub> orbital and five iron 4*d* orbitals. The  $\sigma_{\text{C-H}}$  and  $\sigma_{\text{C-H}}^*$  orbitals of the substrate were not incorporated into the active-space because of limited electron correlation effects between the two orbitals that don't need to be treated at the full configuration-interaction level. While for the transition states (TSs) the doubly occupied  $\sigma_{\text{CHO}}$  orbital and the corresponding antibonding orbital  $\sigma_{\text{CHO}}^*$  are necessary owing to the three-center interaction (C-H-O) that develops in the TSs. A active space of CAS(14,11) including five Fe 3*d* based orbitals, the three oxygen *p*-orbitals, the bonding counterpart of the Fe-*d*<sub>x<sup>2</sup>-y<sup>2</sup></sub> orbital,  $\sigma_{\text{CHO}}$  and  $\sigma_{\text{CHO}}^*$  was therefore constructed. In addition, to account for the double-shell effect, as was accounted for the RCs, it is necessary to add the iron 4*d* shell on top of CAS(14,11). However, the resulting active-space, CAS(14,16), became too large to compute with the usual CASSCF calculations. Therefore, to make a balance between size and accuracy we added three iron 4*d* orbitals (*d*<sub>xy</sub>, *d*<sub>xz</sub>, *d*<sub>yz</sub>) to correlate the important *t*<sub>2g</sub> set of electrons and an active space of CAS(14,14) results. The CASSCF/NEVPT2 reaction barriers were therefore calculated using the CASSCF(12,14)/NEVPT2 and CASSCF(14,14)/NEVPT2 energies for RCs and TSs, respectively. The solvent and thermal corrections and the entropy terms to the Gibbs free energy changes ( $\Delta G$ ) were obtained from the B3LYP calculations. These corrections are listed in Table S9 in the supporting information.

## ASSOCIATED CONTENT

### Supporting Information.

Supplemental Figures on experimental results described in the text, details about CASSCF and DFT calculations, additional information on the reaction energetics for CHD and DHA substrates and optimized Cartesian coordinates of all the species. This material is available free of charge via the Internet at <http://pubs.acs.org>.

## AUTHOR INFORMATION

### Corresponding Authors

\*E-mail: franc.meyer@chemie.uni-goettingen.de

\*E-mail: shengfa.ye@cec.mpg.de

### Notes

The authors declare no competing financial interest.

## ACKNOWLEDGMENT

Support by the Fonds der Chemischen Industrie (Kekulé-Scholarship for C.K.), the Deutsche Forschungsgemeinschaft (IRTG 1422 "Metal Sites in Biomolecules: Structures, Regulation and Mechanisms") and COST Action CM1003 (ECOSTBio, STSM at UdG, Spain for C.K.) is gratefully acknowledged. B.M., F.N. and S.Y. gratefully acknowledge financial support from the Max-Planck society.

## REFERENCE

- (1) (a) Krebs, C.; Fujimori, D. G.; Walsh, C. T.; Bollinger, J. M. *Acc. Chem. Res.* **2007**, *40*, 484–492; (b) Nam, W. *Acc. Chem. Res.* **2007**, *40*, 522–531. (c) Que, L. Jr. *Acc. Chem. Res.* **2007**, *40*, 493–500.
- (2) (a) McDonald, A. R.; Que, L., Jr. *Coord. Chem. Rev.* **2013**, *257*, 414–428; (b) Nam, W.; Lee, Y.-M.; Fukuzumi, S. *Acc. Chem. Res.* **2014**, *47*, 1146–1154; (c) Oloo, W. L.; Que, L., Jr., *Acc. Chem. Res.* **2015**, *48*, 2612–2621; (d) Nam, W. *Acc. Chem. Res.* **2015**, *48*, 2415–2423.
- (3) (a) Hong, S.; So, H.; Yoon, H.; Cho, K.-B.; Lee, Y.-M.; Fukuzumi, S.; Nam, W. *Dalton Trans.* **2013**, *42*, 7842–7845. (b) Kaizer, J.; Klinker, E. J.; Oh, N. Y.; Rohde, J.-U.; Song, W. J.; Stubna, A.; Kim, J.; Münck, E.; Nam, W.; Que, L., Jr. *J. Am. Chem. Soc.* **2004**, *126*, 472–473. (c) Comba, P.; Fukuzumi, S.; Kotani, H.; Wunderlich, S. *Angew. Chem., Int. Ed.* **2010**, *49*, 2622–2625. (d) England, J.; Martinho, M.; Farquhar, E. R.; Frisch, J. R.; Bominaar, E. L.; Münck, E.; Que, L., Jr. *Angew. Chem., Int. Ed.* **2009**, *48*, 3622–3626. (e) Lacy, D. C.; Gupta, R.; Stone, K. L.; Greaves, J.; Ziller, J. W.; Hendrich M. P.; Borovik, A. S. *J. Am. Chem. Soc.* **2010**, *132*, 12188–12190.
- (4) Janardanan, D.; Wang, Y.; Schyman, P.; Que, L., Jr.; Shaik, S. *Angew. Chem. Int. Ed.* **2010**, *49*, 3342–3345.
- (5) Xue, G.; De Hont, R.; Münck, E.; Que, L., Jr. *Nat. Chem.* **2010**, *2*, 400–405.
- (6) England, J.; Guo, Y.; Van Heuvelen, K. M.; Cranswick, M. A.; Rohde, G. T.; Bominaar, E. L.; Münck, E.; Que, L., Jr. *J. Am. Chem. Soc.* **2011**, *133*, 11880–11883.
- (7) (a) Seo, M. S.; Kim, N. H.; Cho, K.-B.; So, J. E.; Park, S. K.; Clémancey, M.; Garcia-Serres, R.; Latour, J.-M.; Shaik, S.; Nam, W. *Chem. Sci.* **2011**, *2*, 1039–1045. (b) Biswas, A. N.; Puri, M.; Meier, K.K.; Oloo, W.N.; Rohde, G.T.; Bominaar, E. L.; Münck, E.; Que, L., Jr. *J. Am. Chem. Soc.* **2015**, *137*, 2428–2431. (c) Bae, S.H.; Seo, M.S.; Lee, Y.-M.; Cho, K.-B.; Kim, W.-S.; Nam, Wonwoo *Angew. Chem. Int. Ed.* **2016**, *55*, 8027–8031.
- (8) (a) Andris, E.; Jašík, J.; Gómez, L.; Costas, M.; Roithová, J. *Angew. Chem. Int. Ed.* **2016**, *55*, 3637–3641. (b) Andris, E.;

- Navrátil, R.; Jasík, J.; Thibault, T.; Srnc, M.; Costas, M.; Roithová, J. *J. Am. Chem. Soc.* **2017**, *139*, 2757–2765.
- (9) (a) Shaik, S.; Hirao, H.; Kumar, D. *Acc. Chem. Res.* **2007**, *40*, 532–542. (b) Hirao, H.; Que, L., Jr.; Nam, W.; Shaik, S. *Chem. Eur. J.* **2008**, *14*, 1740–1756.
- (10) (a) Mandal, D.; Ramanan, R.; Usharani, D.; Janardanan, D.; Wang, B.; Shaik, S. *J. Am. Chem. Soc.* **2015**, *137*, 722–733. (b) Mandal, D.; Shaik, S. *J. Am. Chem. Soc.* **2016**, *138*, 2094–2097.
- (11) (a) England, J.; Prakash, J.; Cranswick, M. A.; Mandal, D.; Guo, Y.; Münck, E.; Shaik, S.; Que, L., Jr. *Inorg. Chem.* **2015**, *54*, 7828–7839. (b) Kwon, Y. H.; Mai, B. K.; Lee, Y. M.; Dhuri, S. N.; Mandal, D.; Cho, K. B.; Kim, Y.; Shaik, S.; Nam, W. *J. Phys. Chem. Lett.* **2015**, *6*, 1472–1476.
- (12) Meyer, S.; Klawitter, I.; Demeshko, S.; Bill, E.; Meyer, F. *Angew. Chem. Int. Ed.* **2013**, *52*, 901–905.
- (13) Rohde, J.-U.; In, J.-H.; Lim, M. H.; Brennessel, W. W.; Bukowski, M. R.; Stubna, A.; Münck, E.; Nam, W.; Que, L., Jr. *Science* **2003**, *299*, 1037–1039.
- (14) Ye, S.; Kupper, C.; Meyer, S.; Andris, E.; Navrátil, R.; Krahe, O.; Mondal, B.; Atanasov, M.; Bill, E.; Roithová, J.; Meyer, F.; Neese, F. *J. Am. Chem. Soc.* **2016**, *138*, 14312–14325.
- (15) Jackson, T. A.; Rohde, J.-U.; Seo, M. S.; Sastri, C. V.; DeHont, R.; Ohta, T.; Kitagawa, T.; Münck, E.; Nam, W.; Que, L., Jr.; Stubna, A. *J. Am. Chem. Soc.* **2008**, *130*, 12394–12407.
- (16) Decker, A.; Rohde, J.-U.; Klinker, E. J.; Wong, S. D.; Que, L., Jr.; Solomon, E. I. *J. Am. Chem. Soc.* **2007**, *129*, 15983–15996.
- (17) Cho, K.-B.; Hirao, H.; Shaik, S.; Nam, W. *Chem. Soc. Rev.* **2016**, *45*, 1197–1210.
- (18) Kleespies, S. T.; Oloo, W. N.; Mukherjee, A.; Que, L., Jr. *Inorg. Chem.* **2015**, *54*, 5053–5064.
- (19) Luo, Y.-R. Handbook of Bond Dissociation Energies in Organic Compounds; CRC Press LLC: Boca Raton, FL, 2003.
- (20) Sastri, C. V.; Lee, J.; Oh, K.; Lee, Y. J.; Lee, J.; Jackson, T. A.; Ray, K.; Hirao, H.; Shin, W.; Halfen, J. A.; Kim, J.; Que, L., Jr.; Shaik, S.; Nam, W. *Proc. Natl. Acad. Sci.* **2007**, *104*, 19181–19186.
- (21) Planas, O.; Clémancey, M.; Latour, J.-M.; Company, A.; Costas, M. *Chem. Commun.* **2014**, *50*, 10887–10890.
- (22) (a) Bell, R. P. *Proc. R. Soc. London, Ser. A* **1936**, *154*, 414–429. (b) Evans, M. G.; Polanyi, M. *Trans. Faraday Soc.* **1938**, *34*, 11–23.
- (23) The error of this KIE value was derived from several experiments and error bars for each individual  $k_{\text{obs}}$  value. Because of the very slow reactions with deuterated substrates at low temperatures, the differences in rate for the different concentrations of DHA- $d_4$  are relatively large compared to the experimental error in the determination of  $k_{\text{obs}}$  values, resulting in a rather high uncertainty for the KIE.
- (24) Price, J. C.; Barr, E. W.; Tirupati, B.; Bollinger, M., Jr.; Krebs, C. *Biochemistry* **2003**, *42*, 7497–7508.
- (25) Nesheim, J. C.; Lipscomb, J. D. *Biochemistry* **1996**, *35*, 10240–10247.
- (26) (a) Kwart, H. *Acc. Chem. Res.* **1982**, *15*, 401–408. (b) Knapp, M. J.; Klinman, J. P. *Eur. J. Biochem.* **2002**, *269*, 3113–3121. (c) Wang, Q.; Sheng, X.; Horner, J. H.; Newcomb, M. et al., *J. Am. Chem. Soc.* **2009**, *131*, 10629–10636. (d) Klinman, J. P., *Chem. Phys. Lett.* **2009**, *471*, 179–193.
- (27) Company, A.; Prat, I.; Frisch, J. R.; Mas-Ballesté, R.; Güell, M.; Juhász, G.; Ribas, X.; Münck, E.; Luis, J. M.; Que, L. Jr.; Costas, M. *Chem. Eur. J.* **2011**, *17*, 1622–1634.
- (28) (a) Geng, C.; Ye S.; Neese, F. *Angew. Chem., Int. Ed.* **2010**, *49*, 5717; (b) Cho, K.-B.; Wu, X.; Lee, Y.-M.; Kwon, Y. H.; Shaik, S.; Nam W. *J. Am. Chem. Soc.* **2012**, *134*, 20222; (c) Rana, S.; Dey, A.; Maiti, D. *Chem. Commun.* **2015**, *51*, 14469–14472.
- (29) (a) Parsell, T. H.; Behan, R. K.; Green, M. T.; Hendrich, M. P.; Borovik, A. S., *J. Am. Chem. Soc.* **2006**, *128*, 8728–8729. (b) Parsell, T. H.; Yang, M.-Y.; Borovik, A. S., *J. Am. Chem. Soc.* **2009**, *131*, 2762–2763. (c) Chen, J.; Lee, Y.-M.; Davis, K. M.; Wu, X.; Seo, M. S.; Cho, K.-B.; Yoon, H.; Park, Y. J.; Fukuzumi, S.; Pushkar, Y. N.; Nam, W., *J. Am. Chem. Soc.* **2013**, *135*, 6388–6391. (d) Garcia-Bosch, I.; Company, A.; Cady, C. W.; Styring, S.; Browne, W. R.; Ribas, X.; Costas, M., *Angew. Chem. Int. Ed.* **2011**, *50*, 5648–5653. (e) Wang, D.; Ray, K.; Collins, M. J.; Farquhar, E. R.; Frisch, J. R.; Gómez, L.; Jackson, T. A.; Kerscher, M.; Waleska, A.; Comba, P.; Costas, M.; Que, L. Jr. *Chem. Sci.* **2013**, *4*, 282–291.
- (30) Dunitz, J. D., *Chem. Biol.* **1995**, *2*, 709–712.
- (31) Collins, T. J.; Ryabov, A. D. *Chem. Rev.* DOI: 10.1021/acs.chemrev.7b00034
- (32) (a) Warren, J. J.; Tronic, T. A.; Mayer, J. M., *Chem. Rev.* **2010**, *110*, 6961–7001. (b) Geng, C.; Ye, S.; Neese, F. *Dalton Trans.* **2014**, *43*, 6079–6086.
- (33) (a) Harvey, J. N. *Annu. Rep. Prog. Chem., Sect. C: Phys. Chem.* **2006**, *102*, 203–226. (b) Ghosh, A. *J. Biol. Inorg. Chem.* **2006**, *11*, 712–724. (c) Pierloot, K.; Vancoillie, S. *J. Chem. Phys.* **2006**, *125*, 124303. (d) Pierloot, K.; Vancoillie, S. *J. Chem. Phys.* **2008**, *128*, 034104. (e) Vancoillie, S.; Zhao, H.; Radon, M.; Pierloot, K. *J. Chem. Theory Comput.* **2010**, *6*, 576–582.
- (34) Altun, A.; Breidung, J.; Neese, F.; Thiel, W. *J. Chem. Theory Comput.* **2014**, *10*, 3807–3820.
- (35) (a) Roos, B. O. *Adv. Chem. Phys.* **1987**, *69*, 399–445. (b) Ruedenberg, K.; Cheung, L. M.; Elbert, S. T. *Int. J. Quantum Chem.* **1979**, *16*, 1069–1101. Ross, B. O.; Taylor, P. R.; Siegbahn, P. E. M. *Chem. Phys.* **1980**, *48*, 157–173.
- (36) Angeli, C.; Cimiraaglia, R.; Evangelisti, S.; Leininger, T.; Malrieu, J. P. *J. Chem. Phys.* **2001**, *114*, 10252–10264.
- (37) Ye, S.; Xue, G.; Krivokapic, I.; Petrenko, T.; Bill, E.; Que, L., Jr.; Neese, F. *Chem. Sci.* **2015**, *6*, 2909–2921.
- (38) (a) Jannuzzi, S. A. V.; Phung, Q. M.; Domingo, A.; Formiga, A. L. B.; Pierloot, K. *Inorg. Chem.* **2016**, *55*, 5168–5179. (b) Alcover-Fortuny, G.; Caballol, R.; Pierloot, K.; de Graaf, C. *Inorg. Chem.* **2016**, *55*, 5274–5280.
- (39) Pierloot, K.; Phung, Q. M.; Domingo, A. *J. Chem. Theory Comput.* **2017**, *13*, 537–553.
- (40) (a) Mondal, B.; Roy, L.; Neese, F.; Ye, S. *Isr. J. Chem.* **2016**, *56*, 763–772. (b) Ye, S.; Neese, F. *Proc. Natl. Acad. Sci.* **2011**, *108*, 1228–1233.
- (41) (a) Ye, S.; Neese, F. *Curr. Op. Chem. Biol.* **2009**, *13*, 89–98. (b) Shaik, S.; Chen, H.; Janardanan, D. *Nat. Chem.* **2010**, *3*, 19–27.
- (42) Malrieu, J. P.; Guihéry, N.; Calzado, C. J.; Angeli, C. *J. Comput. Chem.* **2006**, *28*, 35–50.
- (43) Pierloot, K. *Mol. Phys.* **2003**, *101*, 2083–2094.
- (44) Grimme, S.; Ehrlich, S.; Goerigk, L. *J. Comput. Chem.* **2011**, *32*, 1456–1465.
- (45) Siegbahn, P. E. M. *J. Biol. Inorg. Chem.* **2006**, *11*, 695–701.
- (46) Anneser, M. R.; Haslinger, S.; Pöthig, A.; Cokoja, M.; Basset, J.-M.; Kühn, F. E. *Inorg. Chem.* **2015**, *54*, 3797–3804.
- (47) Cantú Reinhard, F. G.; de Visser, S. P. *Chem. Eur. J.* **2017**, *23*, 2935–2944.
- (48) Bernasconi, L.; Baerends, E. J. *Eur. J. Inorg. Chem.* **2008**, 1672–1681.
- (49) (a) Andersson, K.; Malmqvist, P.-Å.; Roos, B. O.; Sadlej, A. J.; Wolinski, K. *J. Phys. Chem.* **1990**, *94*, 5483–5488. (b) Andersson, K.; Malmqvist, P.-Å.; Roos, B. O. *J. Chem. Phys.* **1992**, *96*, 1218–1226.
- (50) Verma, P.; Vogiatzis, K. D.; Planas, N.; Borycz, J.; Xiao, D. J.; Long, J. R.; Gagliardi, L.; Truhlar, D. G. *J. Am. Chem. Soc.* **2015**, *137*, 5770–5781.
- (51) Johansson, A. J.; Blomberg, M. R. A.; Siegbahn, P. E. M. *J. Phys. Chem. C* **2007**, *111*, 12397–12406.
- (52) Lundberg, M.; Siegbahn, P. E. M. *J. Chem. Phys.* **2005**, *122*, 224103.
- (53) Harvey, J. N. *WIREs Comput. Mol. Sci.* **2013**, *4*, 1–14.
- (54) (a) Lehnert, N.; Ho, R. Y. N.; Que, L., Jr.; Solomon, E. I. *J. Am. Chem. Soc.* **2001**, *123*, 8271–8290. (b) Decker, A.; Rohde, J.-U.;

1  
2 Que, L., Jr.; Solomon, E. I. *J. Am. Chem. Soc.* **2004**, *126*, 5378 -  
3 5379. (c) Neese, F. *J. Inorg. Biochem.* **2006**, *100*, 716 - 726. (d)  
4 Bernasconi, L.; Louwerse, M. J.; Baerends, E. J. *Eur. J. Inorg. Chem.*  
5 **2007**, 3023–3033. (e) Kumar, D.; Karamzadeh, B.; Sastry, G. N.; de  
6 Visser, S. P. *J. Am. Chem. Soc.* **2010**, *132*, 7656–7667.

7 (55) (a) Neidig, M. L.; Decker, A.; Choroba, O. W.; Huang, F.;  
8 Kavana, M.; Moran, G. R.; Spencer, J. B.; Solomon, E. I. *Proc. Natl.*  
9 *Acad. Sci.* **2006**, *103*, 12966–12973. (b) Srnc, M.; Wong, S. D.;  
10 England, J.; Que, L., Jr.; Solomon, E. I. *Proc. Natl. Acad. Sci.* **2012**,  
11 *109*, 14326–14331. (c) Mai, B. K.; Kim, Y. *Inorg. Chem.* **2016**, *55*,  
12 3844–3852.

13 (56) (a) Ye, S.; Geng, C.-Y.; Shaik, S.; Neese, F. *Phys. Chem.*  
14 *Chem. Phys.* **2013**, *15*, 8017–8030. (b) Dietl, N.; Schlangen, M.;  
15 Schwarz, H. *Angew. Chem., Int. Ed.* **2012**, *51*, 5544 - 5555.

16 (57) (a) Kumar, D.; Hirao, H.; Que, L.; Shaik, S. *J. Am. Chem. Soc.*  
17 **2005**, *127*, 8026–8027. (b) Hirao, H.; Kumar, D.; Que, L., Jr.; Shaik,  
18 S. *J. Am. Chem. Soc.* **2006**, *128*, 8590–8606.

19 (58) Macikenas, D.; Skrzypczak-Jankun, E.; Protasiewicz, J. D. *J.*  
20 *Am. Chem. Soc.* **1999**, *121*, 7164–7165.

21 (59) Neese, F. *WIREs Comput. Mol. Sci.* **2012**, *2*, 73–78.

22 (60) (a) Becke, A. D. *Phys. Rev. A* **1988**, *38*, 3098–3100. (b) Lee,  
23 C.; Yang, W.; Parr, R. G. *Phys. Rev. B* **1988**, *37*, 785–789.

24 (61) Schäfer, A.; Huber, C.; Ahlrichs, R. *J. Chem. Phys.* **1994**, *100*,  
25 5829.

26 (62) Schäfer, A.; Horn, H.; Ahlrichs, R. *J. Chem. Phys.* **1992**, *97*,  
27 2571.

28 (63) (a) van Lenthe, E.; Baerends, E. J.; Snijders, J. G. *J. Chem.*  
29 *Phys.* **1993**, *99*, 4597–4610. (b) van Lenthe, E.; Baerends, E. J.;  
30 Snijders, J. G. *J. Chem. Phys.* **1994**, *101*, 9783–9792. (c) van Lenthe,  
31 E.; van Leeuwen, R.; Baerends, E. J.; Snijders, J. G. *Int. J. Quantum*  
32 *Chem.* **1996**, *57*, 281–293.

33 (64) Neese, F.; Wennmohs, F.; Hansen, A.; Becker, U. *Chem.*  
34 *Phys.* **2009**, *356*, 98–109.

35 (65) Tomasi, J.; Mennucci, B.; Cammi, R. *Chem. Rev.* **2005**, *105*,  
36 2999–3094.

37 (66) Weigend, F.; Ahlrichs, R. *Phys. Chem. Chem. Phys.* **2005**, *7*,  
38 3297.

## Table of Contents artwork

